

# Nanoscale

Accepted Manuscript



This is an *Accepted Manuscript*, which has been through the Royal Society of Chemistry peer review process and has been accepted for publication.

*Accepted Manuscripts* are published online shortly after acceptance, before technical editing, formatting and proof reading. Using this free service, authors can make their results available to the community, in citable form, before we publish the edited article. We will replace this *Accepted Manuscript* with the edited and formatted *Advance Article* as soon as it is available.

You can find more information about *Accepted Manuscripts* in the [Information for Authors](#).

Please note that technical editing may introduce minor changes to the text and/or graphics, which may alter content. The journal's standard [Terms & Conditions](#) and the [Ethical guidelines](#) still apply. In no event shall the Royal Society of Chemistry be held responsible for any errors or omissions in this *Accepted Manuscript* or any consequences arising from the use of any information it contains.

Contact angle of a nanodrop on a nanorough solid  
surface

Gersh O. Berim and Eli Ruckenstein\*

*Department of Chemical and Biological Engineering,*

*State University of New York at Buffalo,*

*Buffalo, New York 14260*

---

\*Author to whom correspondence should be addressed. Electronic mail: feaeliru@buffalo.edu; Phone number: (716)645-1179; Fax: (716)645-3822.

## Abstract

The contact angle of a cylindrical nanodrop on a nanorough solid surface is calculated, for both hydrophobic and hydrophilic surfaces, using the density functional theory. The emphasis of the paper is on the dependence of the contact angle on roughness. The roughness is modeled by rectangular pillars of infinite length located on the smooth surface of a substrate, with fluid-pillar interactions different in strength from the fluid-substrate ones. It is shown that for hydrophobic substrates the trend of the contact angle to increase with increasing roughness, which was noted in all previous studies, is not universally valid, but depends on the fluid-pillar interactions, pillar height, interpillar distance, as well as on the size of the drop. For hydrophilic substrate, an unusual kink-like dependence of the contact angle on the nanodrop size is found which is caused by the change in the location of the leading edges of the nanodrop on the surface. It is also shown that the Wenzel and Cassie-Baxter equations can not explain all the peculiarities of the contact angle of a nanodrop on a nanorough surface.

## 1 Introduction

For more than two centuries, the behavior of a macroscopic liquid drop on a solid surface was the object of great practical and theoretical interests. The three basic equations employed are the Young equation [1]

$$\gamma_{lv} \cos \theta = \gamma_{sv} - \gamma_{sl} \quad (1)$$

for smooth surfaces as well as the Wenzel equation [2]

$$\cos \theta_W = r \cos \theta \quad (2)$$

and Cassie-Baxter equation [3]

$$\cos \theta_{CB} = f \cos \theta + f - 1 \quad (3)$$

for rough surfaces. In the above equations,  $\theta$ ,  $\theta_W$ , and  $\theta_{CB}$  are the contact angles on a smooth surface, a rough surface in which the liquid penetrates into the space between asperities (Wenzel regime), and a rough surface in which the space beneath the drop is filled with air (Cassie-Baxter regime). In addition,  $\gamma_{lv}$ ,  $\gamma_{sv}$ , and  $\gamma_{sl}$  are the liquid-vapor, solid-vapor, and solid-liquid surface tensions, respectively,  $r$  is the roughness defined as the ratio between the actual area of the rough surface and the projected area of this surface onto a horizontal smooth one, and  $f$  is the roughness defined as the ratio between the top area of asperities and the area of the surface free of asperities.

Because the surface tensions as well as  $r$  and  $f$  do not depend on the drop size and shape, eqs 1, 2, and 3 predict that the contact angle of a macroscopic drop is independent of the drop size. Another feature is related to the dependence of the contact angle on the roughness of the surface. For both Wenzel and Cassie-Baxter regimes, the contact angle increases with increasing roughness if the solid substrate is hydrophobic ( $\theta > 90^\circ$ ) and decreases if it is hydrophilic ( $\theta < 90^\circ$ ). (Below, the terms hydrophobic and hydrophilic will be used for any surface-fluid pairs, not only for the surface-water one).

Even though in most cases eqs 1-3 provide correct descriptions of the experimental data, some cases were identified for which the above mentioned characteristics are not valid. First, it was observed that for small spherical drops (microdrops) on a smooth surface the contact angle depends on the radius  $R$  of the contact line between drop and surface. In this case, the Young equation has to be modified by introducing a term involving the ratio between the line tension  $\tau$  and radius  $R$ . The modified equation has the form [4]

$$\gamma_{lv} \cos \theta = \gamma_{sv} - \gamma_{sl} - \frac{\tau}{R}. \quad (4)$$

Eq 4 coincides with eq 1 in the limit  $R \rightarrow \infty$  (large drop). However, for a cylindrical (two-dimensional) drop, i.e. a drop which is elongated in a single direction, the last term in eq 4 should not occur because the contact line between the drop and solid is a straight line ( $R = \infty$ ). Therefore,  $\theta$  for a cylindrical drop does not depend on the drop size.

The situation becomes more complex when the drop size becomes of the order of a few nanometers. In this case, the thickness of the liquid-fluid interface between the core of the drop and surrounding vapors becomes comparable with the drop size and the macroscopic concept of surface tension is no longer valid. For this reason, eqs 1-3 are not applicable to such drops and microscopic considerations are required to describe a nanodrop on a solid surface. Comparatively few studies of nanodrops on nanorough surfaces have been carried out [5]-[11]. In Refs. [5, 10], the calculations were performed using a lattice DFT approach, which is appropriate for three-dimensional nanodrops with heights of up to about  $100\sigma_{ff}$ , where  $\sigma_{ff}$  is the diameter of a fluid molecule. The off lattice DFT approach was employed in Refs. [6, 8, 11]. Because of a large increase of the computational time

for large nanodrops the heights of the considered cylindrical nanodrops were restricted to the range  $10\sigma_{ff}$ - $20\sigma_{ff}$ . In Ref. [7, 9] molecular dynamic simulations were used for drops with heights of several nanometers.

As expected, in many cases the behavior of the contact angles of nanodrops on nanorough surfaces was different from that described by eqs 1-3. As an example, one can mention the qualitative disagreement between the  $r$ -dependence of angle  $\theta$  for a nanodrop on a nanorough hydrophilic surface provided by the Wenzel equation and that provided by molecular dynamics simulation [7] and DFT [8]. In the latter cases,  $\theta$  increases with increasing roughness, whereas eq 2 predicts the opposite behavior.

Porcheron et.al. [5] and Malanoski et.al [10], have noted that on a hydrophobic smooth surface the contact angle increases with increasing size of the drop from about  $10\sigma_{ff}$  to  $120\sigma_{ff}$ , after which it remains constant. That behavior of  $\theta$  was attributed to the line tension. A nonmonotonous dependence of  $\theta$  on the size of the cylindrical drop on a rough hydrophilic surface was also noted [6].

Surprisingly, the behavior of the contact angle of a nanodrop on a nanorough hydrophobic surface agrees qualitatively with the predictions of eqs 1-3. In particular, in Refs. [5]-[7], [10] was noted that on such surfaces angle  $\theta$  increases with increasing roughness, in agreement with eqs 2 and 3. However, in the cases presented in Refs. [5]-[7], [10], the material of the pillars was selected the same as that of the substrate. Is this conclusion also valid when the interactions between fluid and substrate and between fluid and pillars are different? In this paper it is shown that in the latter cases the contact angle of a nanodrop on a rough hydrophobic substrate depends on roughness differently

from the predictions provided by the Wenzel and Cassie-Baxter equations. Along with hydrophobic substrates, the hydrophilic ones are also considered.

## 2 Background

### 2.1 The system and interaction potentials

The considered system (see Figure 1) consists of a one-component fluid of fixed average density  $\rho_{av}$  inside a rectangular box which has finite dimensions  $L_x$  and  $L_h + \sigma_{fs}$  in the horizontal ( $x$ ) and vertical ( $h$ ) directions, respectively, and infinite dimension in the  $y$ -direction perpendicular to the plane of the figure. (The length  $\sigma_{fs}$  is the hard core diameter of the fluid-substrate interaction.) The system is in contact with a rough solid surface which is composed of a semiinfinite uniform substrate having a smooth surface decorated with evenly distributed rectangular pillars which model the roughness. The material of the pillars can be different from that of the substrate. The pillars have heights  $h_p$ , widths  $d_p$ , and distance between their centers  $D_p$ . The parameters of all materials as well as the size of the pillars will be specified below. At the distance  $L_h + \sigma_{fs}$  from the substrate, the system is limited by a hard wall which has no attractive interactions with the fluid molecules. In the horizontal direction along the  $x$  axis, a periodic boundary condition is assumed. It will be assumed that the fluid density distribution (FDD)  $\rho_f(\mathbf{r})$  in the system is uniform in the  $y$ -direction and non-uniform in the  $x$ - and  $h$ -directions i.e.  $\rho_f(\mathbf{r}) \equiv \rho_f(x, h)$ .

The interactions between fluid molecules, between fluid molecules and molecules of

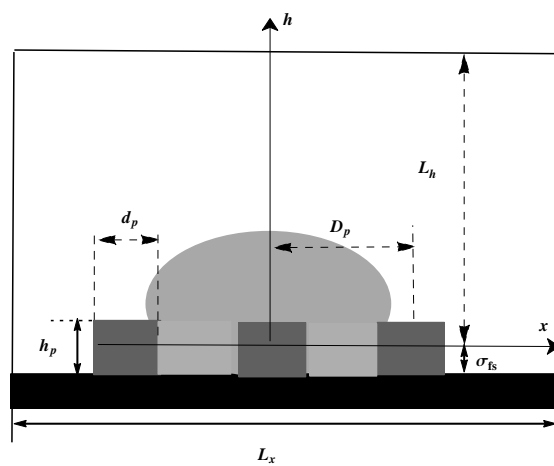


Figure 1: Schematic representation of the considered system. The distances between surfaces are measured between the centers of the molecules forming the first layers.

the substrate and those of the pillars are provided by the Lennard-Jones potential with hard core repulsion

$$\phi_{\alpha}(r) = \begin{cases} 4\epsilon_{\alpha} \left[ \left( \frac{\sigma_{\alpha}}{r} \right)^{12} - \left( \frac{\sigma_{\alpha}}{r} \right)^6 \right], & r \geq \sigma_{\alpha} \\ \infty, & r < \sigma_{\alpha} \end{cases} \quad (5)$$

where  $r = |\mathbf{r} - \mathbf{r}'|$ ,  $\mathbf{r}$  and  $\mathbf{r}'$  provide the locations of the interacting molecules, the subscripts  $\alpha$  are  $ff$ ,  $fs$ , and  $fp$  for fluid-fluid, fluid-substrate, and fluid-pillar interactions, respectively,  $\epsilon_{ff}$ ,  $\epsilon_{fs}$ , and  $\epsilon_{fp}$  are energy parameters, and  $\sigma_{ff}$ ,  $\sigma_{fs}$ , and  $\sigma_{fp}$  are hard core diameters.

For the fluid-fluid interaction, the energy parameter and hard core diameter were selected as for argon ( $\epsilon_{ff}/k_B = 119.76\text{K}$ ,  $\sigma_{ff} = 3.405\text{\AA}$ ) [12], where  $k_B$  is the Boltzmann constant. The substrate-fluid interaction  $\epsilon_{fs}$  was selected  $0.6\epsilon_{ff}$  and  $1.28\epsilon_{ff}$  for hydrophobic and hydrophilic substrates, respectively, with the hard core diameter  $\sigma_{fs} = 3.727\text{\AA}$  the same for both substrates. (The contact angles for a nanodrop on smooth hydrophobic and hydrophilic substrates were  $121^{\circ}$  and  $44^{\circ}$ , respectively [13]). For fluid-pillar interaction the hard core diameter was selected as for the fluid-substrate one ( $\sigma_{fp} = \sigma_{fs}$ ), but the energy parameter  $\epsilon_{fp}$  was varied. The number densities of the substrate and pillars were taken the same  $\rho_s = 1.91 \times 10^{28}\text{m}^{-3}$ . The temperature was selected  $T = 87.0\text{K} = 0.66T_c$ , where  $T_c = 131.6\text{K}$  is the critical temperature of the bulk fluid [12].

The external potential  $U_{fs}$  generated by the solid (substrate plus pillars) does not depend on the coordinate  $y$ , i.e.  $U_{fs} \equiv U_{fs}(x, h)$ . This potential can be calculated by integrating the Lennard-Jones potential (eq 5) for the fluid-substrate and fluid-pillar

interactions over the volume of the substrate and pillars, respectively, and can be written in the form

$$U_{fs}(\mathbf{r}) = \int_{V_s} \rho_s(\mathbf{r}') \phi_{fs}(|\mathbf{r} - \mathbf{r}'|) d\mathbf{r}' + \int_{V_p} \rho_p(\mathbf{r}') \phi_{fp}(|\mathbf{r} - \mathbf{r}'|) d\mathbf{r}' \quad (6)$$

where  $V_s$  and  $V_p$  are the volumes occupied by the substrate and pillars, respectively,  $\rho_s(\mathbf{r}')$  and  $\rho_p(\mathbf{r}')$  are the densities of the substrate and pillars, respectively, which, in general, depend on coordinates. For a uniform substrate ( $\rho_s(\mathbf{r}') \equiv \rho_s = \text{const}$ ) the first integral in eq 6 has the form

$$\int_{V_s} \rho_s(\mathbf{r}') \phi_{fs}(|\mathbf{r} - \mathbf{r}'|) d\mathbf{r}' = \frac{2\pi}{3} \epsilon_{fs} \rho_s \sigma_{fs}^3 \left[ \frac{2}{15} \left( \frac{\sigma_{fs}}{\sigma_{fs} + h} \right)^9 - \left( \frac{\sigma_{fs}}{\sigma_{fs} + h} \right)^3 \right]. \quad (7)$$

The integration of the second part of eq 6 can be carried out analytically only over the  $y$ -coordinate. The integration over the  $x$ - and  $h$ -coordinates was performed numerically. Note that the origin of the coordinate system was selected at the distance  $\sigma_{fs}$  from the substrate surface (see Figure 1).

## 2.2 Basic equation of DFT and its solution

The basic equation for the FDD  $\rho_f(\mathbf{r})$  was obtained by minimizing the Helmholtz free energy of the system,  $F[\rho_f(\mathbf{r})]$ . An explicit expressions for  $F[\rho_f(\mathbf{r})]$  is provided in Appendix A.

As a result of minimization, one obtains the following Euler-Lagrange equation [6]

$$\log[\Lambda^3 \rho_f(x, h)] - Q_f(x, h) = \frac{\lambda}{k_B T} \quad (8)$$

where the function  $Q_f(x, h)$ , which is a functional of  $\rho_f(x, h)$ , is provided in Appendix A,  $\Lambda = h_P/(2\pi mk_B T)^{1/2}$  is the thermal de Broglie wavelength,  $h_P$  is the Planck constant,  $m$  is the mass of a fluid molecule, and  $\lambda$  is a Lagrange multiplier which accounts for the constraint of fixed average density of the fluid. This constraint provides the equation

$$\rho_{av} = \frac{1}{V} \int_V d\mathbf{r} \rho_f(\mathbf{r}) \quad (9)$$

where  $V$  is the volume occupied by the fluid. Eq 9 leads to the following expression for  $\lambda$  [6]

$$\lambda = -k_B T \log \left[ \frac{1}{\rho_{av} V \Lambda^3} \int_V d\mathbf{r} e^{Q_f(x, h)} \right] \quad (10)$$

which after combining with eq 8 provides an integral Euler-Lagrange equation for the FDD  $\rho_f(x, h)$ . The latter equation can be solved numerically by iterations. The details of the iteration procedure are presented in Appendix A. Here we emphasize only the choice of the initial fluid density distribution (initial guess) used in the calculations. Due to the symmetry of the system, it is natural to assume that a nanodrop on a rough surface can exist only in two states which differ by the drop position with respect to the pillars (see Figure 2 where those states are presented schematically). One of them ( $D1$ ) is symmetrical with respect to a vertical plane passing through the middle of the pillar, the second one ( $D2$ ) is symmetrical with respect to a vertical plane located midway between pillars. For this reason, the initial density distribution was usually selected as a cylindrical (two-dimensional) rectangular drop of a reasonable density elongated in the

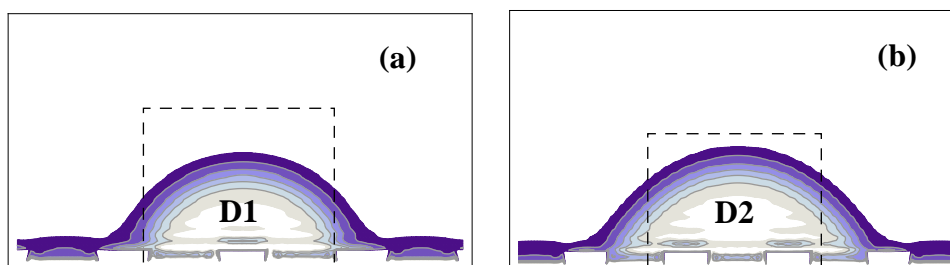


Figure 2: Schematic representation of two possible solutions of the Euler-Lagrange equation. The dashed rectangles represent an initial guess for the iteration procedure. In the figure, the pillars have white color.

$y$ -direction which possesses the symmetry of one of the mentioned above drops. Note that the location of the initial guess at any other position increases the time of calculation but results, nevertheless, in one of the above mentioned two solutions.

As expected, depending on the selected parameters of the system, there are several possible outcomes of the iterations. In the first case, the drop does not form. This occurs when the amount of fluid in the system is too small to ensure a drop existence, or when the solid-fluid interaction is so strong that the fluid molecules completely wet the surface. In the second case, two initial guesses provide finally the same drop ( $D1$  or  $D2$ ). In the last, third case, the initial guesses mentioned above converge to different drops, the free energy of the system being different for the two drops. The drop corresponding to the smaller free energy is considered as stable, the other one as metastable.

When using a numerical procedure to solve the Euler-Lagrange equation, one always encounter the question whether the selected precision can ensure that the obtained solution is not an intermediate step of the iteration procedure, which, in reality, leads to

another solution. We do not have an exact answer to this question. In Appendix B a qualitative approach is presented for handling this uncertain situation.

In conclusion of this section, let us note that the selected temperature,  $T = 87.0\text{K}$ , is far enough from the critical temperature,  $T_c$  of the considered fluid ( $T/T_c = 0.66$ ) for the thermal fluctuations to be small. For this reason, the use of DFT, which is based on a mean-field approximation for the fluid-fluid interactions, is justified.

### 2.3 Calculation of the contact angle

Because of the nonuniformity of the fluid in nanodrops, the drop profile needed to calculate the contact angle, is not clearly defined. In this paper, a simple procedure is used in which the drop profile is given by the line in the vapor-liquid interface which corresponds to a local constant density  $\rho_{div}$ . The procedure how to determine  $\rho_{div}$  was described in Ref. [14]. An example of a drop profile obtained in this way is presented in Figure 3. On this figure and all similar figures below, the lighter areas correspond to higher fluid densities. After the drop profile was obtained, its upper part was approximated by a circle and extrapolated until it intersected the solid. The angle that this circle makes with the solid was considered as the contact angle. This definition of the contact angle does not account for the profile of the drop in the very vicinity of the solid. Close to the solid, the fluid density in the drop has an oscillatory behavior and changes considerable. This makes impossible the use of this region for meaningful contact angle calculations.

Note that in some cases the drop profile has the shape of a closed loop which does not intersect the solid surface. In this case, the contact angle was considered to be  $180^\circ$ .

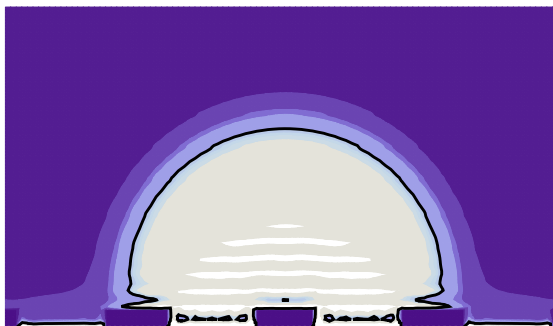


Figure 3: Example of the drop profile (solid line) obtained by the method described in Ref. [14]. The dividing density  $\rho_{div}\sigma_{ff}^3 = 0.375$  in this example. The lighter areas correspond to higher densities.

Using the obtained drop profile one can calculate the number of molecules in the drop  $N_d$  (per unit length) which will be used as a characteristic of the drop size.

### 3 Results and discussion

The characteristics of nanodrops (size, contact angle) were examined for 12 rough surfaces which differ in the distance between pillars and their height. Depending on those parameters, the surfaces have different roughnesses,  $r$ , which were calculated using the equation [8]

$$r = 1 + \frac{2h_p}{D_p} . \quad (11)$$

The notations which will be used to identify the surfaces are presented in Table 1 along with their roughnesses. In most calculations, the total number  $N_{tot}$  of molecules of fluid in the system per unit length in the  $y$ -direction was selected between  $N_{tot}\sigma_{ff} = 80$  and

Table 1: Notations for selected surfaces and their roughnesses

$D_p/\sigma_{ff}$	$h_p/\sigma_{ff}$		
	1	2	3
14.0	$S_{11}$ r=1.143	$S_{12}$ r=1.286	$S_{13}$ r=1.429
9.3	$S_{21}$ r=1.215	$S_{22}$ r=1.430	$S_{23}$ r=1.645
7.5	$S_{31}$ r=1.267	$S_{32}$ r=1.533	$S_{33}$ r=1.800
4.8	$S_{41}$ r=1.417	$S_{42}$ r=1.833	$S_{43}$ r=2.250

$N_{tot}\sigma_{ff} = 180$ . The parameter  $\epsilon_{fp}$  of the fluid-pillar interaction was varied between  $\epsilon_{fp} = 0.20\epsilon_{fs}$  and  $\epsilon_{fp} = 6.0\epsilon_{fs}$  for a hydrophobic substrate and between  $\epsilon_{fp} = 0.05\epsilon_{fs}$  and  $2.0\epsilon_{fs}$  for a hydrophilic one. In all considered cases, the fluid penetrated into the space between pillars (the Wenzel regime).

In Sec. 3.1 it is shown that, for some values of the interaction parameters and size of the drop, the system can be in a stable or metastable state. The dependence of the contact angle of a nanodrop on a rough surface on the drop size is examined in Sec. 3.2, its dependence on the distance between pillars and their height is presented in Sec. 3.3. Sec. 3.4 is concerned with the effect of fluid-pillar interactions.

### 3.1 Stable and metastable solutions

As already mentioned, two solutions of the Euler-Lagrange equation were identified in most cases. One of these solutions corresponds to a global minimum in the Helmholtz free energy (stable state), and the other one corresponds to a local minimum (metastable state). The formalism employed in the present paper allows one to calculate the free energies of those minima and discriminate between stable and metastable states. However it does not allow to obtain the height of the energy barrier, which separates the stable from the metastable state. To make the considerations more general, it will be assumed that the metastable states have enough long lifetimes and for this reason they will be examined along with the stable states.

Because the Euler-Lagrange equation provides solutions corresponding to the extremum of the free energy (minimum or maximum) there is, in principle, the possibility for the state with greater free energy to correspond to a local maximum of the free energy which is, in fact, not metastable but unstable. Another possibility is that the numerically obtained solution is only an intermediate step in the sequence of iterations which eventually lead to a stable solution if a higher calculation precision would have been used. Those issues are examined in Appendix B.

The stability and metastability of the drops on rough surfaces depend on a number of factors and it is difficult to formulate general rules for their identification. Some specific results for drops  $D1$  and  $D2$  on a hydrophobic substrate with pillars of height  $h_p = \sigma_{ff}$  and  $\epsilon_{fp} = \epsilon_{fs}$  are presented in Table 2 for  $N_{tot}\sigma_{ff}$  between 80 and 180. In the examples

Table 2: The dependence of the state of drops  $D1$  and  $D2$  on rough hydrophobic substrates on the total number  $N_{tot}$  of fluid molecules per unit length of the system. In the considered examples the substrate is decorated with pillars of the same material ( $\epsilon_{fp} = \epsilon_{fs}$ );  $h_p = \sigma_{ff}$ . In the bistable states, the stable and metastable states have the same free energies.

Surface	$N_{tot}\sigma_{ff}$	$D1$	$D2$
$S_{11}$	80-180	metastable	stable
$S_{21}$	80-140	metastable	stable
	150-180	stable	metastable
$S_{31}$	80-110	metastable	stable
	120-180	stable	metastable
$S_{41}$	80-100	metastable	stable
	110	bistable	bistable
	120-180	stable	metastable

listed in Table 2, both drops  $D1$  and  $D2$  are presented for all considered  $N_{tot}$ . However for other choices of the fluid-pillar energy parameter  $\epsilon_{fp}$ , there are cases in which only drop  $D1$  exists and drop  $D2$  is unstable. This happens, for example, for the hydrophilic surface  $S_{21}$  with  $N_{tot} \leq 90$  and  $\epsilon_{fp}/\epsilon_{fs} \leq 0.75$ .

One can see from Table 2, that on surfaces  $S_{21}$ ,  $S_{31}$ , and  $S_{41}$ , the state of the drop (stable or metastable) depends on the number of molecules in the system and as a consequence, on the size of the drop. A possible reason for such a behavior is the change in the location of the leading edges of the drops with respect to pillars. In Figure 4, the drops  $D1$  and  $D2$  are presented for surface  $S_{21}$  and  $N_{tot}\sigma_{ff} = 100$  (first row) and 150 (second row). In the first case, the leading edges of both drops are located on the pillars, with the

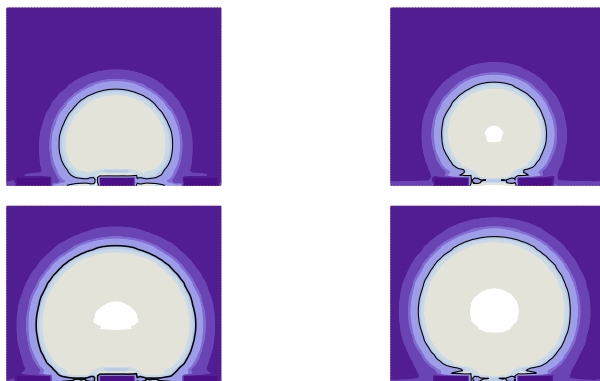


Figure 4: Drops  $D1$  (first column) and  $D2$  (second column) for the systems with  $N_{tot}\sigma_{ff} = 100$  (first row) and  $N_{tot}\sigma_{ff} = 150$  (second row) on the hydrophobic surface  $S_{21}$ .  $\epsilon_{fp}/\epsilon_{fs} = 1$ .

free energy of drop  $D2$  smaller (stable drop) than that of drop  $D1$  (metastable drop). For the greater  $N_{tot}$ , the leading edges of  $D1$  are located between pillars where the attraction by the substrate is larger, whereas those for  $D2$  remain on the pillars. In this case, the free energy of  $D1$  is smaller than that of  $D2$  and  $D1$  is stable while  $D2$  metastable. For surface  $S_{11}$ , for which the distance between pillars is larger than that for  $S_{21}$ , and  $S_{31}$ , the leading edges of  $D2$  are between pillars for all considered values of  $N_{tot}$ . The leading edges of  $D1$  are located either on the pillars or between them. In the latter case, the contact area of  $D1$  with the substrate was always less than that for  $D2$ . For this reason,  $D1$  is always metastable and  $D2$  stable.

### 3.2 Size dependence of $\theta$ on rough surfaces

In this section, the dependence of the contact angle of a nanodrop on a nanorough surface is examined as function of the size of the nanodrop expressed via the number  $N_d$  of fluid

molecules in the drop per unit length in the  $y$ -direction. This number was calculated using FDD and the drop profile extracted from FDD (see Sec. 2.3).

In Figure 5, the size dependence of the contact angle of the nanodrop on four hydrophobic surfaces is presented for drops  $D1$  (Figure 5a) and  $D2$  (Figure 5b). The size of the drop was varied between  $N_d\sigma_{ff} = 40$  and  $N_d\sigma_{ff} = 150$ . For drop  $D1$ , the contact angles on surfaces  $S_{11}$  and  $S_{41}$  decrease monotonously with increasing size of the drop, whereas for the drops on surfaces  $S_{21}$  and  $S_{31}$  this dependence passes through a minimum after which the contact angle only slightly increases with increasing drop size. For drop  $D2$ , the contact angles on surfaces  $S_{11}$  and  $S_{21}$  increase monotonously and for the surface  $S_{41}$  it decreases with increasing size of the drop. For surface  $S_{31}$ , the change in contact angle with  $N_d$  is small. For both nanodrops, the contact angles are not constant, hence in contradiction with the predictions of the traditional macroscopic theory. Note that the line tension cannot explain the dependence of  $\theta$  on the drop size because the leading edges of the drop have infinite radius of curvature and the last term in eq 4 should not be present.

All the peculiarities of contact angle behavior can be qualitatively explained considering the location of the leading edges for different drop sizes. As an example, in Figure 6 drops  $D1$  and  $D2$  of different sizes are present on the hydrophobic surface  $S_{21}$ . In the considered range of drop sizes, drop  $D2$  has its leading edges pinned to the edges of neighboring pillars. This pinning prevents the motion of the drop leading edges on the surface of the pillars and causes a monotonous increase of the contact angle with increasing size of the nanodrop (see the curve for  $S_{21}$  in Figure 5b). It is expected, that this increase

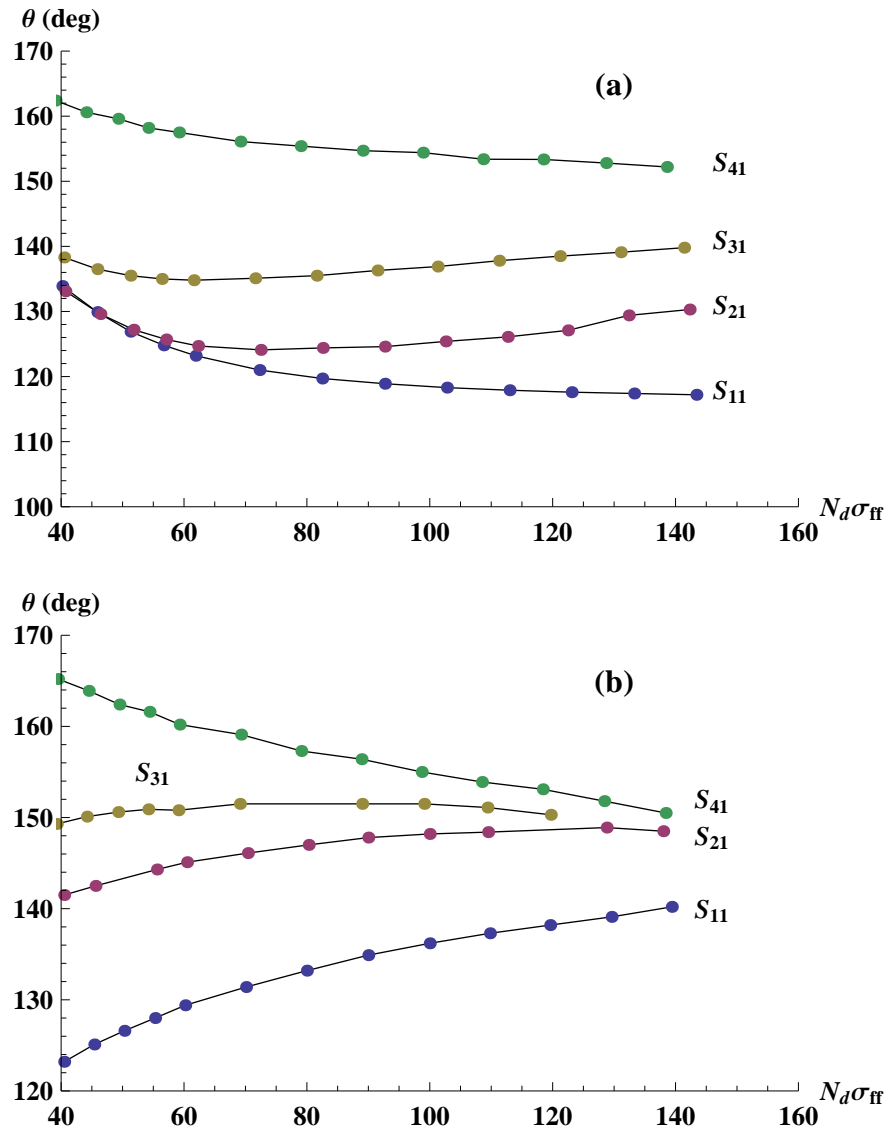


Figure 5: Size dependence of the contact angle of a nanodrop on a rough hydrophobic substrate for  $h_p = \epsilon_{ff}$  for drops  $D1$  (a) and  $D2$  (b) when  $\epsilon_{fp} = \epsilon_{fs}$ . The points represent results of calculations, the curves are guides for eye.

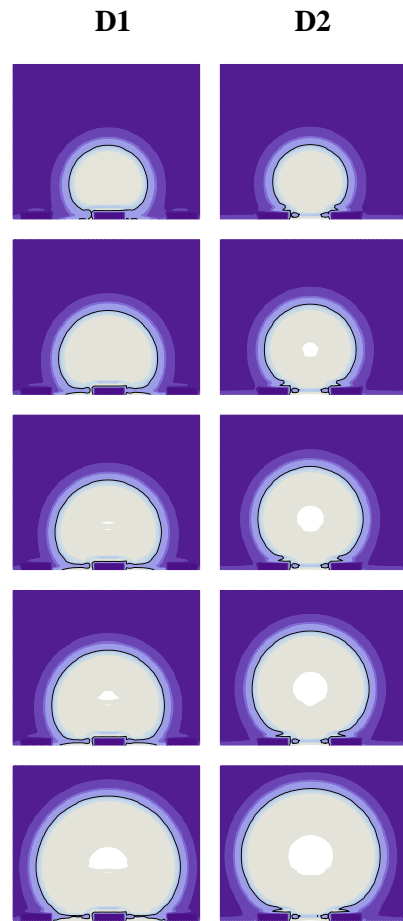


Figure 6: Drops  $D1$  and  $D2$  of various sizes on the hydrophobic surface  $S_{21}$  with  $\epsilon_{fp} = \epsilon_{fs} = 0.6\epsilon_{ff}$ .

will continue until the leading edges of the drop detach from the pillars edges and move on the surface of a pillar toward the next edge of the pillar. For this reason, the width of the drop base increases and the contact angle decreases. The change from the increase of  $\theta$  to its decrease means that there is a local maximum in the dependence of  $\theta$  on the drop size and suggests that the shape of the curve for  $S_{21}$  in Figure 5b should be convex. Note that the suggested maximum is not present in Figure 5b because the required drop size was not achieved in the calculations due to the small size of the system.

For the smallest size of drop  $D1$ , its leading edges are pinned to the edges of the pillar on which the drop is sitting. When the size of the drop increases, the drop leading edges will change their position by moving on the surface of the substrate where the attractive drop-substrate interactions are stronger. This leads to the decrease of the contact angle with increasing drop size until the leading edges become located close to the neighboring pillars and are pinned to them. This is followed by a contact angle increase with increasing drop size as it was in the case of drop  $D2$ . Hence, the size dependence of  $\theta$  for drop  $D1$  should have a minimum (see the curve for  $S_{21}$  in Figure 5a) and the curve for  $S_{21}$  in Figure 5a is convex downward. Note that the changes in contact angle in the used example are small and cannot be detected by eye in Figure 6.

The size dependence of the contact angle on a rough hydrophilic substrate presented in Figure 7 demonstrates a more complex behavior. For drop  $D1$  (Figure 7a), the contact angles on surfaces  $S_{21}$  and  $S_{31}$  first increase with increasing size, then rapidly decrease after which they increase again. As for hydrophobic surfaces, this behavior is related to the change in the location of the leading edges of the drop profile on the surface. Before

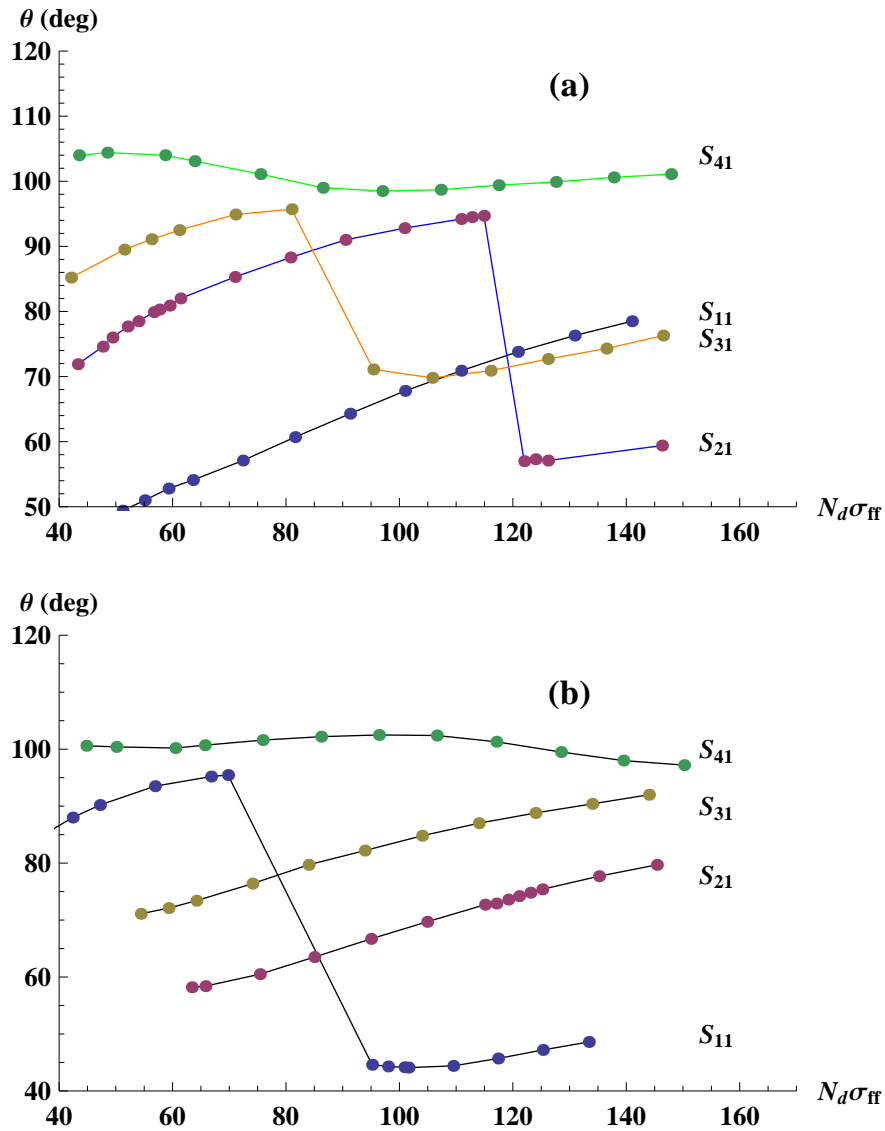


Figure 7: Size dependence of the contact angle of a nanodrop on a rough hydrophilic substrate with  $h_p = \sigma_{ff}$  for drops  $D1$  (a) and  $D2$  (b) when  $\epsilon_{fp} = \epsilon_{fs}$ . The points represent results of calculations, the lines are the guides for eye.

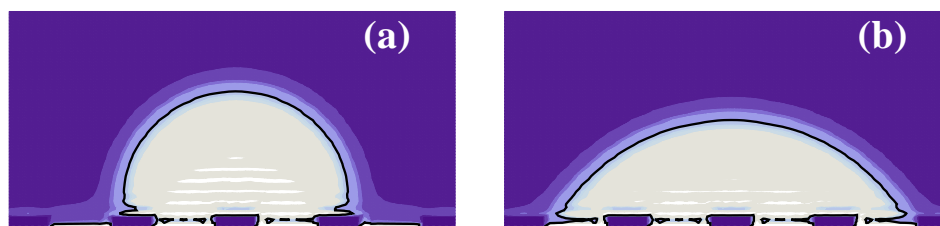


Figure 8: Two characteristic shapes of nanodrop  $D1$  on a rough hydrophilic surface.

$\theta$  decreases, the leading edges are located on the pillars (as shown in Figure 8a) and are pinned to the edges of the pillars. As long as the size of the drop increases up to a critical value, the contact angle increases because the pinning prevents the drop leading edges to move to the space between pillars. At the critical size, the leading edges separate from pillars edges and become located between pillars (Figure 8b). In this case, the contact angle becomes considerably smaller than in the previous case thus explaining the kink-like behavior.

A similar behavior of the contact angle occurs for drop  $D2$  on surface  $S_{11}$  (see Figure 7b).

For drop  $D1$  on the hydrophilic surfaces  $S_{11}$  and  $S_{41}$ , as well as for drop  $D2$  on surfaces  $S_{12}$ ,  $S_{31}$ , and  $S_{41}$  the leading edges of the drop are located either on the pillars or between pillars for all considered drop sizes. For this reason, kink-like changes in the contact angle dependence on  $N_d$  do not occur for those surfaces. Nevertheless, one can expect kinks for larger drop sizes because of changes in the location of the leading edges. However the sizes of these systems do not allow to perform calculations for large nanodrops to identify those kinks.

Note that the absence of such kinks for hydrophobic substrates (Figure 5) can be explained by the lower drop-substrate and drop-pillar interactions compared with the hydrophilic surfaces. As a result, the pinning force is smaller than for hydrophilic surfaces and the change in the contact angle is much smoother when the drop leading edges move from pillars to the space between them.

The dependence of the contact angle on drop size was also examined in connection with the phenomenon of contact angle hysteresis in Ref. [15] by minimizing the free energy of the system, (the latter involving the surface tension), and in Ref. [9] by molecular dynamic simulations. In Ref. [15], the sizes of the considered two-dimensional drops were much larger than the size of the pillars; in Ref. [9], where only three dimensional drops were considered, the sizes of the droplets were comparable to those of the pillars and of the order of a few nanometers. In both papers, kink-like changes in the contact angle with increasing drop volume were identified in some cases that agree with our results obtained by DFT.

Note in conclusion that for both hydrophilic and hydrophobic surfaces the size dependence of the contact angle should be quasiperiodic because the drop leading edges sequentially move along the upper surface of the pillars and along the surface of the substrate, the contact angle being determined by the location of the leading edges of the drop.

### 3.3 Dependence of the contact angle on the distance between pillars and on their height

Examples regarding the dependence of the contact angle of a nanodrop on the distance  $D_p$  between pillars for drop  $D1$  on rough hydrophobic substrate are presented in Figure 9 for surfaces with various pillar heights,  $h_p$ , and strength  $\epsilon_{fp}$  of the fluid-pillar interaction. The roughnesses of the considered surfaces depend both on  $D_p$  and  $h_p$  and are provided above the horizontal axis. In each case, the contact angle first decreases with increasing roughness (decreasing  $D_p$ ) in contradiction with Wenzel equation, but then increases, in qualitative agreement with that equation. Even though  $D_p$ -dependence of  $\theta$  in all considered cases is similar, there are some differences which should be emphasized. For example, for  $h_p/\sigma_{ff} = 1$  and  $h_p/\sigma_{ff} = 2$ , the  $D_p$ -dependencies of  $\theta$  for  $\epsilon_{fp}/\epsilon_{fs} = 3.5$  have minima at different roughnesses 1.27 and 1.43, respectively (compare the dashed lines in Figures 9 (a) and (b)). To explain this observation, let us examine the changes of the drop profiles of drop  $D1$  with changes in the distance between pillars (see Figure 10) for both cases. Comparing the drop profiles for  $h_p/\sigma_{ff} = 1$  and  $h_p/\sigma_{ff} = 2$  one can see that in both cases the contact angle decreases with increasing  $D_p$  as long as the leading edges of the drop remain on the pillars. The contact angle acquires a minimum when  $D_p$  approaches the critical value  $D_{pc}$  at which the leading edges of the drop "jump" from pillars into the area between pillars and the contact angle increases. For  $h_p/\sigma_{ff} = 1$ , the distance  $D_{pc}$  is in the interval  $7.5 < D_{pc}/\sigma_{ff} < 9.3$ . For  $h_p/\sigma_{ff} = 2$ ,  $D_{pc}$  is greater ( $9.3 < D_{pc}/\sigma_{ff} < 14$ ) because the attraction between the leading edges of the drop and

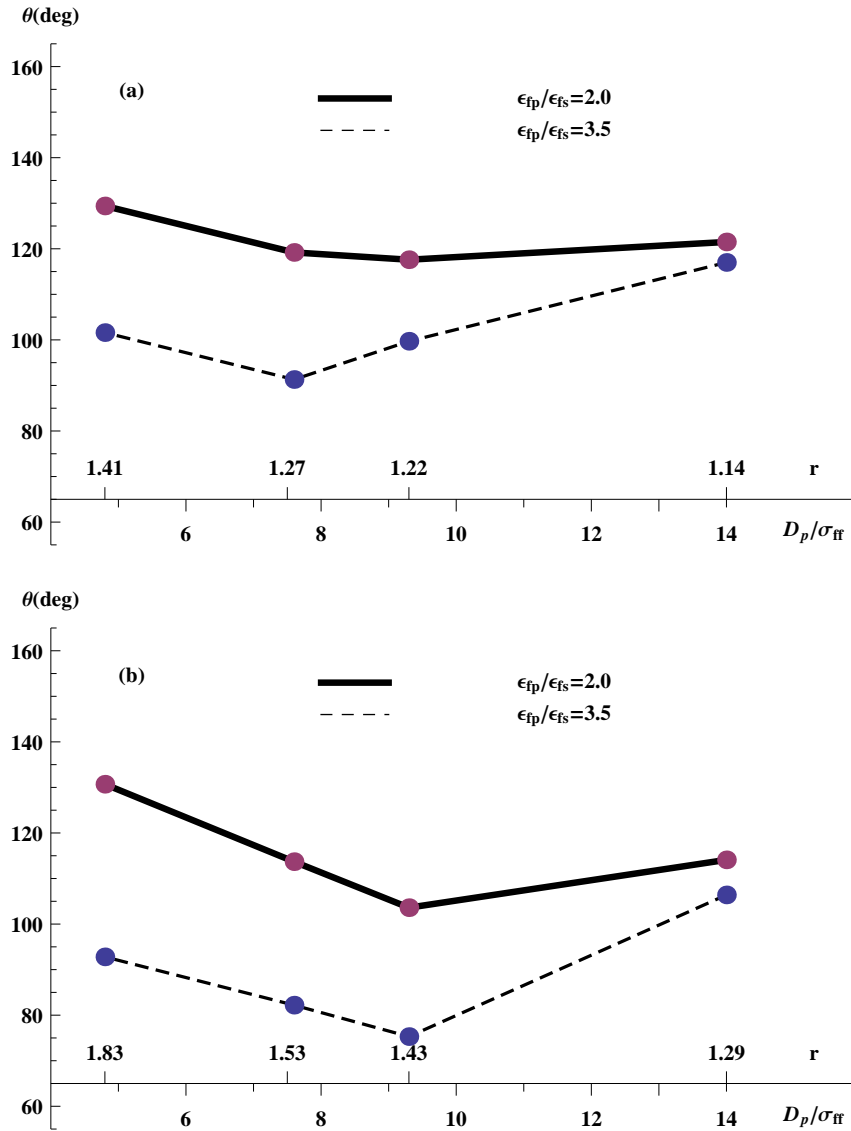


Figure 9: Dependence of the contact angle of drop  $D1$  on a rough hydrophobic substrate on the distance between pillars for  $\epsilon_{fp}/\epsilon_{fs} = 2.0$ , and  $3.5$  for pillars heights  $h_p/\sigma_{ff} = 1$  (a) and  $h_p/\sigma_{ff} = 2$  (b). In all cases  $N_{tot}\sigma_{ff} = 90$ . The points represent results of calculations, the lines are guides for eye.

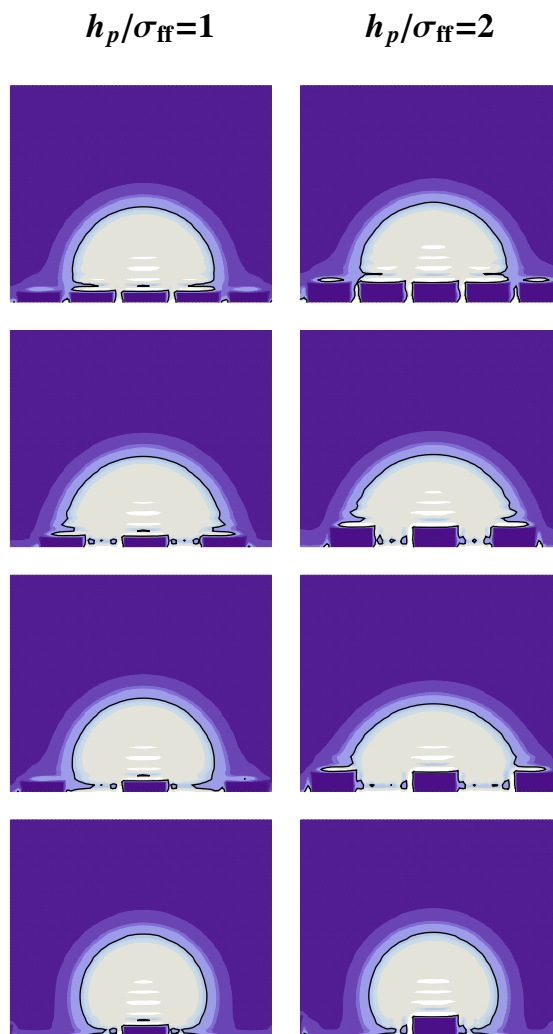


Figure 10: Drops of various sizes on various hydrophobic surfaces decorated with pillars of height  $h_p/\sigma_{ff} = 1$  (first column) and  $h_p/\sigma_{ff} = 2$  (second column). The distances between pillars are  $4.8\sigma_{ff}$  (first row),  $7.5\sigma_{ff}$  (second row),  $9.3\sigma_{ff}$  (third row), and  $14\sigma_{ff}$  (fourth row).  $\epsilon_{fp}/\epsilon_{fs} = 3.5$  for all cases.

the pillars is greater for the larger pillars. For this reason,  $\theta$  exhibits minima at various  $D_p$ . From the above consideration, it is clear that the location of the minimum in the  $D_p$ -dependence of the contact angle depends on the size of the drop and on the strength of fluid-pillar interaction.

Note that the deviation in the contact angle behavior from that predicted by Wenzel equation was noted previously for a nanodrop on a hydrophilic surface [7, 8, 11]. It was, in particular, shown [8] that the contact angle of a nanodrop on a hydrophilic surface increases with increasing roughness, passes through a maximum and then decreases. The latter behavior is in qualitative agreement with eq 2 and eq 3.

For a hydrophobic substrate, the dependence of  $\theta$  on the height of the pillars is presented in Figure 11 for various distances between pillars,  $D_p$ , and energy parameters  $\epsilon_{fp}$ . For most of the considered cases, the contact angle decreases with increasing  $h_p$  (increasing roughness), again in contradiction with eqs 2 and 3. Such a monotonous behavior of  $\theta$  as function of  $r$  differs from that in Figure 9 in which the change in roughness was caused by the change in the distance between pillars.

As expected, the larger  $\epsilon_{fp}$ , the smaller is the contact angle, i.e. the surface becomes less hydrophobic with increasing  $\epsilon_{fp}$ . For the largest  $\epsilon_{fp}$  presented in Figure 11 ( $\epsilon_{fp}/\epsilon_{fs} = 3.5$ ) the surface becomes even hydrophilic ( $\theta < 90^\circ$ ) even though the substrate is hydrophobic. Note that for small distances between pillars (e.g.  $D_p/\sigma_{ff} = 4.8$  in Figure 11), the change in contact angle with the change in their height is much smaller than for the larger values of  $D_p$ . This feature of the contact angle behavior can be understood by taking into account that for small values of  $D_p$  the pillars are close to each other and

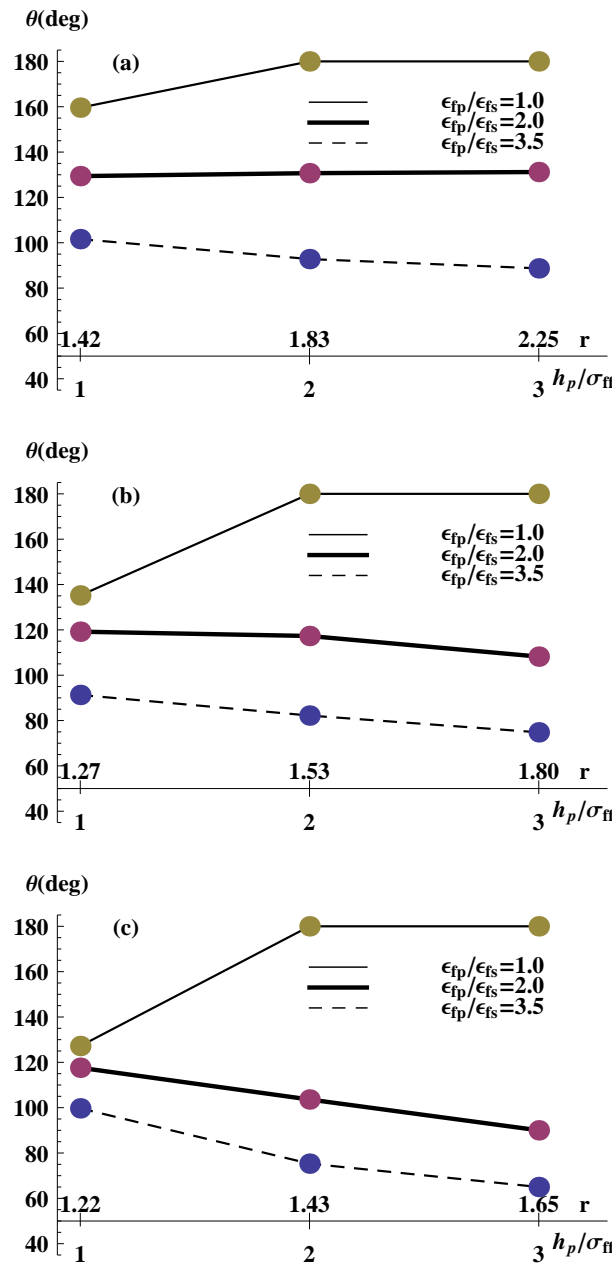


Figure 11: Dependence of the contact angle of drop  $D1$  on a rough hydrophobic substrate on the height of pillars for  $\epsilon_{fp}/\epsilon_{fs} = 1.0, 2.0$ , and  $3.5$  for several surfaces. The distances between pillars are  $4.8\sigma_{ff}$  (a),  $7.5\sigma_{ff}$  (b), and  $9.3\sigma_{ff}$  (c). The roughness  $r$  is provided above the horizontal axis. The points represent results of calculations, the lines are guides for eye. In all cases,  $N_{tot}\sigma_{ff} = 90$ .

form a quasi smooth surface. The interaction of this surface with the fluid molecules is only slightly dependent on the height of the pillars.

All the above considerations indicate that the roughness as defined by eq 11 cannot be considered the appropriate unique characteristics of the wetting of a surface. To provide additional evidence, the contact angle is plotted in Figure 12 as a function of roughness for  $\epsilon_{fp}/\epsilon_{fs} = 3.5$ . One can see that different surfaces (e.g.  $S_{31}$  and  $S_{12}$ ), for which the contact angles are very different (about  $91^\circ$  and  $106^\circ$ , respectively) exhibit approximately the same roughness (1.27 and 1.29, respectively). This is also true for surfaces  $S_{41}$  and  $S_{22}$ . For this reason,  $\theta$  behaves irregularly as function of  $r$  in the range  $r \simeq 1.26$  and  $r = 1.44$  (Figure 12).

### 3.4 Dependence of the contact angle on fluid-pillar interaction

Figure 13 presents the dependence of the contact angle on the strength  $\epsilon_{fp}$  of the fluid-pillar interaction for a hydrophobic substrate decorated with pillars of height  $h_p = \sigma_{ff}$ . As expected,  $\theta$  decreases with increasing  $\epsilon_{fp}$  for both drops,  $D1$  and  $D2$ . In both cases, the change in contact angle when  $\epsilon_{fp}$  is changed from  $\epsilon_{fp}/\epsilon_{fs} = 0.2$  to  $\epsilon_{fp}/\epsilon_{fs} = 6.0$  is the smallest for surface  $S_{11}$ , the change for  $D1$  being smaller than for  $D2$  ( $\Delta\theta_1 \simeq 15^\circ$  and  $\Delta\theta_2 \simeq 55^\circ$ , respectively). Such a difference between  $\Delta\theta_1$  and  $\Delta\theta_2$  occurs because in the first case ( $D1$ ) the leading edges of the drop are located on the substrate and the pillars are beneath the drop (see Figure 6, left column). For drop  $D2$ , the leading edges of the drop are on the pillars and for this reason the pillars affect the contact angle stronger than for  $D1$ , especially for larger  $\epsilon_{fp}/\epsilon_{fs}$ . When the distance between pillars is the smallest

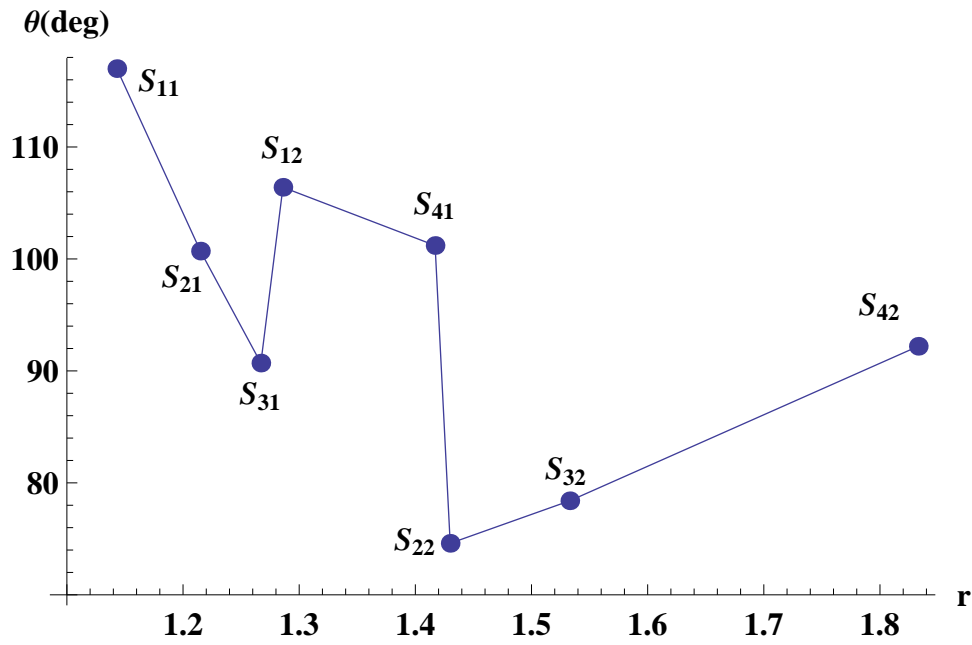


Figure 12: Dependence of the contact angle on roughness for a drop on a rough hydrophobic substrate for  $\epsilon_{fp}/\epsilon_{fs} = 3.5$ . The points represent results of calculations, the lines are guides for eye. The labels at each point indicate the surface used in calculations. In all cases,  $N_{tot}\sigma_{ff} = 90$ .

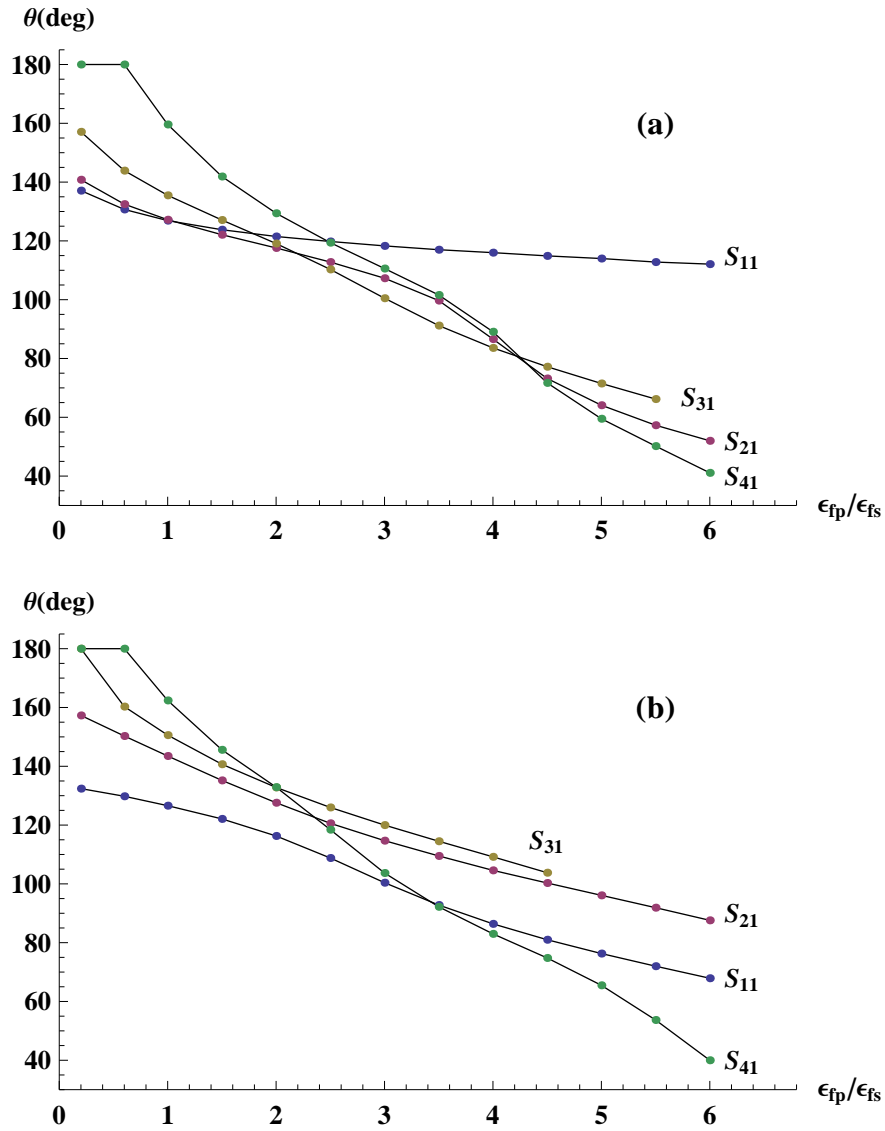


Figure 13: Dependence of the contact angles of drops  $D1$  (a) and  $D2$  (b) on the ratio  $\epsilon_{fp}/\epsilon_{fs}$  for various surfaces in the case of hydrophobic substrates. The points are results of calculations, the lines are guides for eyes. In all cases,  $N_{tot}\sigma_{ff} = 90$ .

(surface  $S_{41}$ ), the number of pillars beneath the drop increases and this causes higher changes in  $\theta$  with changing  $\epsilon_{fp}$ .

## 4 Conclusions

In contrast to macroscopic drops for which the contact angles on smooth and rough surfaces are governed by eqs 1-3 and for which the dependence on drop size and roughness of the surface have some universal features, the contact angle of nanodrops on nanorough surfaces exhibits nonuniversalities both with respect to the drop size and roughness [5]-[10].

In this paper it is shown that depending on the size of the drop as well as on the size and position of the pillars, there is even less universality in the contact angle behavior than it was found previously.

First, the contact angle depends on drop size and such a dependence is absent for macrodrops. In Ref. [10] it was shown that on smooth as well as on rough hydrophobic surfaces the contact angle increases with increasing drop size. Because the drop is three-dimensional, one can assign this behavior to the existence of line tension (see eq 4). In our calculations in which a two-dimensional drop of much smaller size is considered, both an increase and a decrease in the contact angle with increasing drop size was identified. This behavior cannot be related to the line tension because the latter plays no role for two-dimensional drops. In addition, kink-like dependence of the contact angle on drop size was found for rough hydrophilic substrates, which occur when the leading edges of the

drop change their location with respect to the pillars. One can expect that such kinks can repeat with increasing drop size when the leading edges of the drop change their location from on the pillars to between pillars.

In Refs. [5]-[7],[10], the increase of  $\theta$  with increasing roughness of a hydrophobic surface was found to occur in all considered cases, in agreement with the behavior of  $\theta$  for macroscopic drops. Note that in those studies, the condition  $\epsilon_{fp} = \epsilon_{fs}$  was employed. However, for  $\epsilon_{fp} > \epsilon_{fs}$ , we have found cases when the contact angle first decreases with increasing roughness and then increases, as well as cases when the contact angle monotonously decreases with increasing roughness.

On the basis of the previous results and those obtained in the present paper, the conclusion is that the roughness  $r$  alone cannot explain all the peculiarities of the contact angle behavior of nanodrops on rough surfaces. Only a microscopic theory can provide adequate results for any values of the interaction parameters.

In this paper, only the Wenzel regime was considered. To obtain a stable Cassie-Baxter type drop, surfaces with higher hydrophobicity or pillars with larger heights should be examined.

## 5 Appendix A Free energy contributions and solution of the Euler-Lagrange equation

Following Refs. [16, 17], the total Helmholtz free energy  $F[\rho_f(\mathbf{r})]$  of a considered system can be represented as the sum of four contributions. The first one is the ideal gas free

energy

$$F_{id}[\rho_f(\mathbf{r})] = k_B T \int d\mathbf{r} \rho_f(\mathbf{r}) \{ \log[\Lambda^3 \rho_f(\mathbf{r})] - 1 \}, \quad (\text{A. 1})$$

where  $\Lambda = h_P / (2\pi m k_B T)^{1/2}$  is the thermal de Broglie wavelength,  $h_P$  the Planck constant, and  $m$  the mass of a fluid molecule. The second contribution is the free energy of a reference system of hard spheres

$$F_{hs}[\rho_f(\mathbf{r})] = \int d\mathbf{r} \rho_f(\mathbf{r}) \Delta\Psi_{hs}(\mathbf{r}) \quad (\text{A. 2})$$

where

$$\Delta\Psi_{hs}(\mathbf{r}) = k_B T \eta_{\bar{\rho}_f} \frac{4 - 3\eta_{\bar{\rho}_f}}{(1 - \eta_{\bar{\rho}_f})^2}, \quad (\text{A. 3})$$

$\eta_{\bar{\rho}_f} = \frac{1}{6} \pi \bar{\rho}_f(\mathbf{r}) \sigma_{ff}^3$  being the packing fraction of the fluid molecules and  $\bar{\rho}_f(\mathbf{r})$  is a smoothed density defined as

$$\bar{\rho}_f(\mathbf{r}) = \int d\mathbf{r}' \rho_f(\mathbf{r}') W(|\mathbf{r} - \mathbf{r}'|). \quad (\text{A. 4})$$

The weighting function  $W(|\mathbf{r} - \mathbf{r}'|)$  in eq A. 4 is selected in the form [18]

$$W(|\mathbf{r} - \mathbf{r}'|) = \begin{cases} \frac{3}{\pi \sigma_{ff}^3} \left(1 - \frac{r}{\sigma_{ff}}\right), & r \leq \sigma_{ff} \\ 0, & r > \sigma_{ff} \end{cases}$$

where  $r = |\mathbf{r} - \mathbf{r}'|$ . The third contribution is the excess free energy due to fluid-fluid attractive interaction which is accounted for in the mean-field approximation

$$F_{attr}[\rho_f(\mathbf{r})] = \frac{1}{2} \int \int d\mathbf{r} d\mathbf{r}' \rho_f(\mathbf{r}) \rho_f(\mathbf{r}') \phi_{ff}(|\mathbf{r} - \mathbf{r}'|) \quad (\text{A. 5})$$

where  $\phi_{ff}(|\mathbf{r} - \mathbf{r}'|)$  is the Lennard-Jones potential of the fluid-fluid interactions provided by eq 5.

The last contribution is due to the interaction between fluid and solid molecules

$$F_{fs}[\rho_f(\mathbf{r})] = \int_V d\mathbf{r} \rho_f(\mathbf{r}) U_{fs}(\mathbf{r}) \quad (\text{A. 6})$$

where  $V$  is the volume occupied by the fluid, and  $U_{fs}(\mathbf{r})$  is provided by eq 6.

The minimization of the Helmholtz free energy with respect to the fluid density distribution  $\rho_f(x, h)$  leads to the following Euler-Lagrange equation for  $\rho_f(x, h)$ .

$$\log[\Lambda^3 \rho_f(x, h)] - Q_f(x, h) = \frac{\lambda}{k_B T} . \quad (\text{A. 7})$$

In eq A. 7,  $\lambda$  is a Lagrange multiplier and the function  $Q_f(x, h)$  is given by

$$Q_f(x, h) = -\frac{1}{k_B T} \left[ \Delta \Psi_{hs}(x, h) + \overline{\Delta \Psi'}_{hs}(x, h) + U_{ff}(x, h) + U_{fs}(x, h) \right] \quad (\text{A. 8})$$

where

$$U_{ff}(x, h) = \int \int dx' dh' \rho_f(x', h') \phi_{ff,y}(|x - x'|, |h - h'|), \quad (\text{A. 9})$$

$$\overline{\Delta \Psi'}_{hs}(x, h) = \int \int dx' dh' \rho_f(x', h') W_y(|x - x'|, |h - h'|) \frac{\partial}{\partial \bar{\rho}} \Delta \Psi_{hs}(\bar{\rho}) \Big|_{\bar{\rho}=\bar{\rho}_f(x', h')} . \quad (\text{A. 10})$$

The functions  $\phi_{ff,y}(|x-x'|, |h-h'|)$  and  $W_y(|x-x'|, |h-h'|)$  are obtained by integrating the potential  $\phi_{ff}(|\mathbf{r}-\mathbf{r}'|)$  and the weighted function  $W(|\mathbf{r}-\mathbf{r}'|)$  with respect to  $y$  from  $-\infty$  to  $+\infty$ , respectively.

When calculating  $U_{ff}(x, h)$  which is due to the long-range fluid-fluid interactions, a cutoff at a distance equal to four molecular diameters  $\sigma_{ff}$  for the range of Lennard-Jones attraction was employed. The precision of the iterations was characterized by the dimensionless quantity

$$\delta = \int_V dx dh \left[ \rho_{f,i+1}(x, h) - \rho_{f,i}^{in}(x, h) \right]^2 / \left( \int_V dx dh \rho_{f,i}(x, h) \right)^2$$

where  $\rho_{f,i}^{in}(x, h)$  is the input density profile for the  $(i+1)$ -th iteration  $\rho_{f,i+1}(x, h)$ , generated by the Euler-Lagrange equation. The iterations were carried out on a two dimensional grid with a spacing  $0.1\sigma_{ff}$  until  $\delta$  became smaller than  $10^{-7}$ . The cutoff radius of  $4\sigma_{ff}$  was used in the integrations involving the fluid-fluid interactions.

## 6 Appendix B

The obvious way to proof that the solution of the Euler-Lagrange equation (let say, for drop  $D1$ ), obtained with a selected precision, is not an intermediate step in the iteration procedure that eventually will provide the other solution (drop  $D2$ ) is to increase the precision of the calculation. However for the two-dimensional case considered in the present paper this way is impractical because it involves a considerable increase in the calculation time, which even for the selected precision  $\delta = 10^{-7}$  lasts about seven hours. To obtain at least a qualitative answer to the above question, the following procedure was

developed which uses an intrinsic stability criterion for a system which has a minimum in its free energy. First, the obtained density profile  $\rho_f(x, h)$  was disturbed by shifting it in some direction (let say, to the left) by a few grid intervals. This new density distribution,  $\rho'_f(x, h)$ , which now is asymmetric with respect to the initial plane of symmetry, is used as a new initial guess for the Euler-Lagrange equation. If the nonshifted FDD  $\rho_f(x, h)$  provides the minimum (local or global) in the free energy, the iteration procedure which started with  $\rho'_f(x, h)$  should converge to  $\rho_f(x, h)$ . However the absence of symmetry in  $\rho'_f(x, h)$  leads to an extremely slow convergence of the iteration procedure. To obtain the decision more rapidly, track was kept of the difference  $\Delta\rho'_{f,i}(x, h) = \rho'_{f,i+1}(x, h) - \rho'_{f,i}(x, h)$  between the density distributions,  $\rho'_{f,i}(x, h)$  and  $\rho'_{f,i+1}(x, h)$ , provided by two successive iterations started with the initial guess  $\rho'_f(x, h)$ . After 50 - 100 iterations this difference as function of  $x$  and  $h$  has, generally, one of the two shapes presented in Figures 14a, and b, where the light (dark) areas represent positive (negative) values of  $\Delta\rho'_{f,i}(x, h)$ . Figures 14a and b indicate the tendency of the density distribution  $\rho_{f,i}(x, h)$  to “move” in the direction of the positive part of  $\Delta\rho'_{f,i}(x, h)$ , i.e. to the left for Figure 14a and to the right for Figure 14b. If  $\Delta\rho'_{f,i}(x, h)$  had the shape shown in Figure 14a, the unshifted solution was considered unstable and was disregarded. In the opposite case, when  $\Delta\rho'_{f,i}(x, h)$  had the shape shown in Figure 14b, the unshifted solution was considered stable or metastable.

Note that if the initial guess for the iteration procedure is selected at the location of the stable or metastable solution of Euler-Lagrange equation, the difference  $\Delta\rho'_{f,i}(x, h)$  has the symmetric shape shown in Figure 14c.

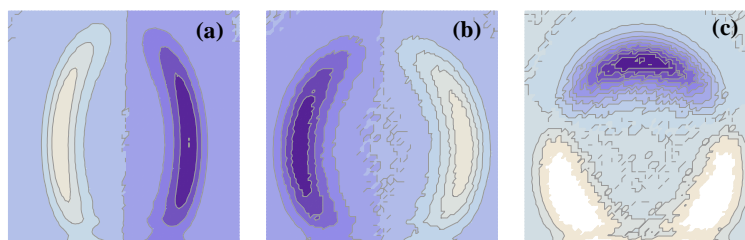


Figure 14: (a), (b), and (c) Possible contour plots of the differences between two consecutive iterations. Dark areas correspond to negative values of the differences and light areas correspond to positive ones.

## References

- [1] T. Young, *Philos. Trans. R. Soc. London*, 1805, **95**, 65-87.
- [2] R.N. Wenzel, *Ind. Eng. Chem.*, 1936, **28**, 988-994.
- [3] A.B.D. Cassie and S. Baxter, *Trans. Faraday Soc.*, 1944, **40**, 0546-0550.
- [4] B.A.Pethica, *Rep. Prog. Appl. Chem.*, 1961, **46**, 14; B.A.Pethica, *J. Colloid Interface Sci.*, 1977, **62**, 567-569.
- [5] F.Porcheron, P.A.Monson and M.Schoen, *Phys.Rev. E*, 2006, **73**, 041603.
- [6] G.O. Berim and E. Ruckenstein, *Journal of Chemical Physics*, 2008, **129**, 014708.
- [7] C.D. Daub, J.H. Wang, S. Kudesia, D. Bratko and A. Luzar, *Faraday Discussions*, 2010, **146**, 67-77.
- [8] G.O. Berim and E. Ruckenstein, *Journal of Colloid and Interface Science*, 2011, **359**, 304-310.

- [9] T.Koishi, K.Yasuoka, S.Fujikawa, and X.C.Zeng, *ACS Nano*, 2011, **5**, 6834-6842.
- [10] A.P. Malanoski, B.J. Johnson and J.S. Erickson, *Nanoscale*, 2014, **6**, 5260-5269.
- [11] A.Malijevsky, *J.Chem.Phys.*, 2014, **141**, 184703.
- [12] R. Evans and P. Tarazona, *Physical Review A*, 1983, **28**, 1864-1868.
- [13] G.O. Berim and E. Ruckenstein, *Journal of Chemical Physics*, 2009, **130**, 044709.
- [14] G.O. Berim and E. Ruckenstein, *Journal of Chemical Physics*, 2008, **129**, 114709.
- [15] H.Kusumaatmaja and J.M.Yeomas, *Langmuir*, 2007, **23**, 6019-6032.
- [16] P. Tarazona, *Physical Review A*, 1985, **31**, 2672-2679.
- [17] P. Tarazona, U.M.B. Marconi and R. Evans, *Molecular Physics*, 1987, **60**, 573-595.
- [18] R.H. Nilson and S.K. Griffiths, *Journal of Chemical Physics*, 1999, **111**, 4281-4290.